Density-controlled reversal of collective migration in bacterial aerotaxis

Dipanjan Ghosh [1,*,†], Brato Chakrabarti [2,‡] and Xiang Cheng [1,3,§]

[1]*Department of Chemical Engineering and Materials Science, University of Minnesota, Minneapolis, Minnesota 55455, USA*

[2]*International Center for Theoretical Sciences, Tata Institute of Fundamental Research, Bengaluru 560089, India*

[3]*St. Anthony Falls Laboratory, University of Minnesota, Minneapolis, Minnesota 55414, USA*

(Received 13 November 2025; accepted 29 April 2026; published 14 July 2026)

In living matter, chemical gradients that populations generate and reshape often guide collective migration. Bacterial aerotaxis exemplifies this feedback between metabolism and movement, giving rise to unexpected collective behaviors. Here, we combine quantitative experiments, theoretical modeling, and numerical simulations to reveal a striking, density-dependent reversal in the migration of *Escherichia coli* within self-generated oxygen gradients. At low cell densities, populations retreat from the oxygen-rich interface; at high densities, they move toward it. A biophysical model in which bacteria bias their motion toward an intermediate, metabolically optimal oxygen concentration quantitatively captures this reversal and predicts a critical density at which collective migration ceases, even in the presence of sustained oxygen gradients. These findings reconcile long-standing discrepancies in observations of bacterial aerotaxis and highlight how feedback between metabolism, movement, and environmental shaping governs emergent behaviors in active matter, with potential implications for microbiome ecology.

DOI: 10.1103/y7l1-288v

I. INTRODUCTION

Self-propelled agents in active living matter can dynamically reshape the very landscapes that guide their motion, creating intricate feedback between movement and environment [1]. Such dynamic coupling underlies diverse processes in biology, from self-organized pattern formation in multicellular systems to collective migration in bacterial populations [2–4]. In particular, bacterial chemotaxis typifies this feedback mechanism [5,6]: chemotactic bacteria migrate along chemical gradients sculpted by secretion [7], consumption [8,9], and motility-induced flows [10].

Among various chemotactic cues, oxygen holds special significance—historically, as the first molecule shown to direct bacterial motion [11–13]; ecologically, as one of the most pervasive in microbial habitats [14]; and biologically, as a central regulator of metabolism and motility [15]. The response of bacterial populations to oxygen gradients—known as *aerotaxis*—has become a central paradigm in the study of biological active matter [16,17], offering key insights into collective migration [18–21], bioconvection [22,23], and bacterial turbulence [24–26].

Despite decades of study, however, experiments on the model aerotactic bacterium *Escherichia coli* (*E. coli*)—a prototypical example of active matter—report contradictory responses. Seminal experiments by Adler [8] and subsequent work by Holz and Chen [27] showed *E. coli* in a capillary formed a traveling band moving toward the air-water interface, whereas later experiments by Douarche *et al.* [28] in the same geometry observed migration in the opposite direction, toward oxygen-depleted regions. How can the same chemical—oxygen—elicit opposite migratory responses in a population of *E. coli*? These opposing results reveal a fundamental gap in understanding the feedback mechanisms that govern collective dynamics in active matter, particularly in bacterial aerotaxis.

In this work, we show that coupling aerotaxis with a self-generated oxygen gradient gives rise to an unusual, density-dependent reversal in the direction of bacterial migration. This switch, driven by a single chemical species, has no analog in classical chemotaxis, where the direction of migration is fixed with cells moving unidirectionally either up or down the chemical gradient [29]. Specifically, we investigate bacterial migration in a capillary channel over a range of population densities. The cells spontaneously form a concentrated band in the channel. At low densities, the band migrates away from the oxygen-rich interface, whereas at high densities, the migration reverses direction and the band moves toward the interface. A kinetic theory based on the hypothesis that *E. coli* seeks an intermediate oxygen level optimal for metabolism reproduces the migration reversal at a critical density. Analysis of a simple model further illustrates the underlying physical mechanisms. The migration reversal arises from the interplay of two dynamical processes: oxygen transport and bacterial aerotactic migration, which define two relevant length

*Contact author: dipanjan.ghosh@ist.ac.at

†Present address: Institute of Science and Technology Austria, Klosterneuburg, Austria.

‡Contact author: brato.chakrabarti@icts.res.in

§Contact author: xcheng@umn.edu

Published by the American Physical Society under the terms of the Creative Commons Attribution 4.0 International license. Further distribution of this work must maintain attribution to the author(s) and the published article's title, journal citation, and DOI.

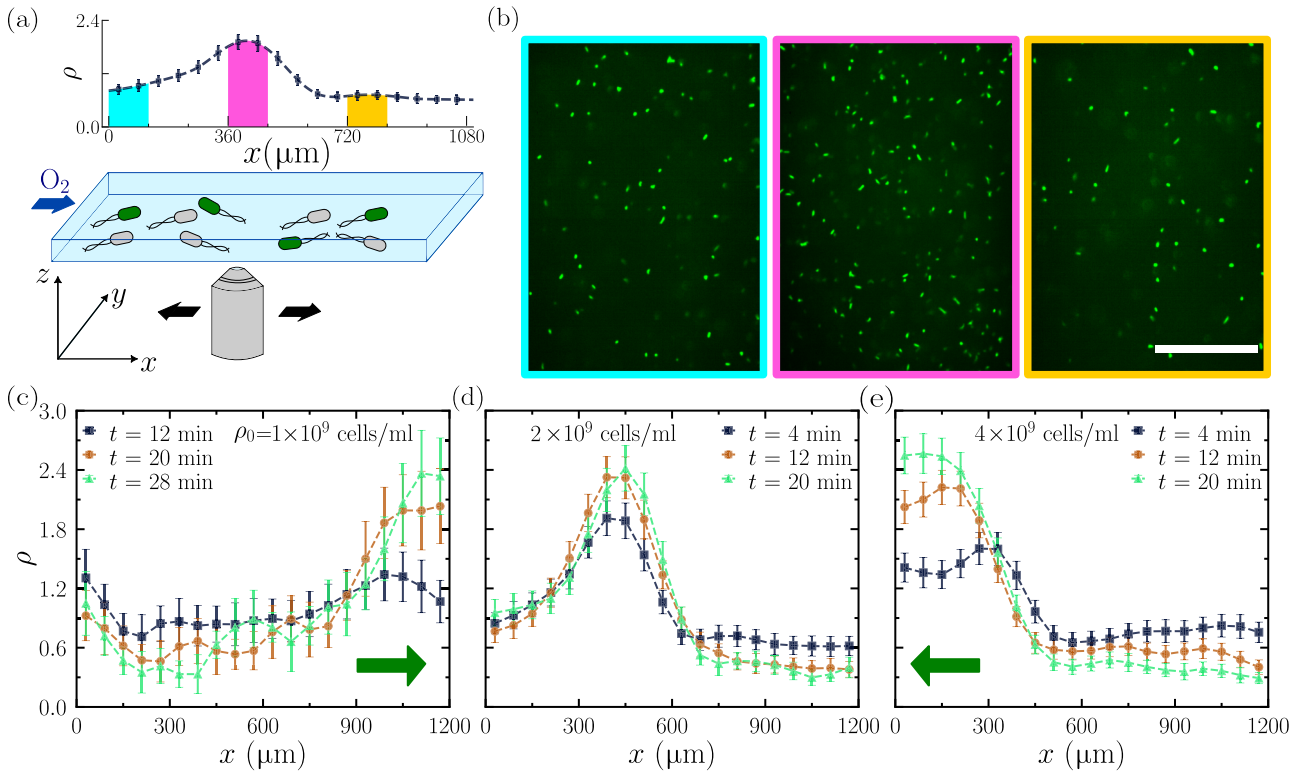

FIG. 1. Bacterial aerotaxis in experiments. (a) Schematic of the experimental setup with a suspension of *E. coli* in a glass capillary channel in contact with atmospheric oxygen at $x = 0$. The objective lens moves along the x direction to record videos at different spatial locations. Top: Spatial bacterial density profile from an experiment with overall cell density $\rho_0 = 2 \times 10^9$ cells/ml at $t = 4$ min. (b) Panels outlined with different colors show snapshots of the suspension at $x = 0$–120, 360–480, and 720–840 μm, corresponding to the shaded regions on the density profile in panel (a). Fluorescently tagged bacteria, imaged using confocal microscopy, appear as bright ellipsoids against a background of nonfluorescent bacteria. The ratio of fluorescent to nonfluorescent cells is 1:4. The scale bar is 50 μm. The temporal variation of bacterial density profiles for $\rho_0 = 1 \times 10^9$ cells/ml [panel (c)], 2×10^9 cells/ml [panel (d)], and 4×10^9 cells/ml [panel (e)]. The migration directions of the bacterial population in panels (c) and (e) are shown using the green arrows. Error bars indicate the standard error.

scales whose relative sizes determine the migration direction. At the critical density where these length scales coincide, migration stalls despite the presence of strong oxygen gradients. Therefore, bacterial density emerges as a control parameter for migration direction, revealing a previously unrecognized feedback-mediated mechanism for self-organization in active matter.

Our paper is organized as follows: Sec. II presents the experimental findings, followed by the kinetic theory in Sec. III. In Sec. IV, we introduce a simple physical model that illustrates the competing factors underlying the migration reversal. The conclusions and physiological implications of our results are discussed in Sec. V.

II. EXPERIMENTS

A. Setup and results

We prepare bacterial suspensions with varying overall cell densities, ρ_0, and introduce these suspensions into a horizontal glass capillary channel with one end open to the atmosphere [Fig. 1(a)]. A subpopulation of the bacterial cells is marked with a fluorescent plasmid, enabling us to track local density and quantify the spatial distribution. Oxygen diffuses from the air-water interface into the channel and is continuously consumed by the bacteria, creating an oxygen gradient with the highest concentration at the interface ($x = 0$). We compute the normalized spatial density profile of bacteria, $\rho(x)$, by counting fluorescently labeled cells at each position [Figs. 1(a) and 1(b)]. Further details of our experimental methods are provided in Appendixes A–C.

We measure the temporal evolution of $\rho(x)$ for different overall bacterial densities, ρ_0. Figures 1(c)–(e) show $\rho(x)$ at multiple time points for three representative values of ρ_0. At early times, we observe the emergence of a high-density peak in $\rho(x)$, i.e., a bacterial band, regardless of ρ_0. The peak appears closer to the interface at larger ρ_0 initially and migrates over time, with its direction of movement depending on ρ_0. At a low density $\rho_0 = 1 \times 10^9$ cells/ml [Fig. 1(c)], bacteria migrate away from the air-water interface toward regions of low oxygen concentrations. In contrast, at a high density $\rho_0 = 4 \times 10^9$ cells/ml [Fig. 1(e)], the peak migrates in the opposite direction toward the air-water interface, where oxygen concentration is highest. At an intermediate density $\rho_0 = 2 \times 10^9$ cells/ml [Fig. 1(d)], the peak position remains nearly stationary.

Quantitatively, we measure the average migration velocity of the bacterial population, v_m, as a function of ρ_0 [Fig. 2(a)] (Appendix D). For each density, measurements were repeated in three independent experiments. The results show a transition in $v_m(\rho_0)$ from interface-directed

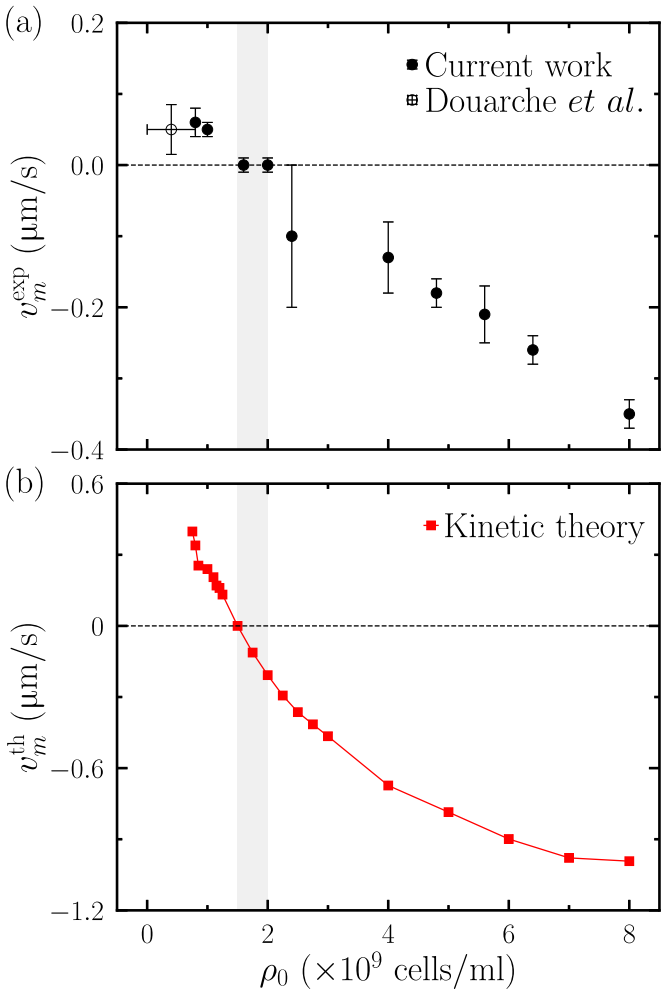

FIG. 2. Migration velocity of the bacterial population as a function of overall bacterial density ρ_0. (a) Experimentally measured migration velocity $v_m^{\rm exp}$. (b) Migration velocity $v_m^{\rm th}$ obtained from kinetic theory. Filled black circles in the top panel show measurements from the present work, while the open circle corresponds to the measurement by Douarche *et al.* [28]. In our study, each data point represents the mean of three independent experiments, and error bars denote the standard error of the mean. The shaded region in both panels indicates the range of bacterial densities (1.5×10^9 to 2.0×10^9 cells/ml) over which experimentally measured migration velocity changes sign.

to bulk-directed migration at a critical density $\rho_c \approx 1.5 \times 10^9$ to 2.0×10^9 cells/ml. Migration becomes faster as ρ_0 deviates further from ρ_c, in either direction.

B. Existing theories

Classical theories of bacterial chemotaxis predict directed migration along chemical gradients, with the direction of migration fixed by the sign of the chemotactic sensitivity. In the context of aerotaxis, Keller-Segel-type continuum models therefore predict accumulation toward regions of higher oxygen concentration when bacteria are attracted to oxygen [30–32]. Such models are consistent with interface-directed migration observed at high densities but are inconsistent with the reversed migration at low densities.

Alternative models emphasize motility modulation rather than directional bias. In particular, Douarche *et al.* proposed a mechanism in which bacterial swimming speed—and hence effective diffusivity—decreases with increasing oxygen concentration, leading to migration away from oxygen-rich regions [28]. Such a mechanism can account qualitatively for migration away from the interface at low densities. However, it does not explain the interface-directed migration observed at high densities. Moreover, when treated consistently—i.e., with no-flux boundary conditions imposed on the full transport dynamics—spatial variations in diffusivity alone cannot sustain a localized interior density peak at steady state in the absence of biased run-and-tumble dynamics [33].

A different theoretical approach was introduced by Mazzag *et al.*, who proposed that bacteria perform aerotaxis toward a preferred oxygen concentration and developed a one-dimensional (1D) model coupling biased motion to oxygen diffusion and consumption [34]. This framework successfully explains the formation and propagation of aerotactic bands in environments where bacteria actively reshape the oxygen field through consumption. In this picture, collective migration arises from the interplay between biased motion toward a preferred oxygen level and the self-generated oxygen gradient.

In contrast to the behavior reported here, Mazzag *et al.* [34] do not invoke bacterial density as an independent control parameter for migration direction and do not probe whether variations in bacterial density alone can qualitatively alter migration behavior under otherwise identical environmental conditions. Moreover, direct quantitative comparison with experiments on run-and-tumble bacteria is limited, since the model is formulated in one dimension, whereas reorientation dynamics and migration are inherently higher dimensional. In higher dimensions, translational diffusion and stochastic reorientations can lead to wall accumulation under reflecting (no-flux) boundary conditions, producing nontrivial spatial distributions that can in turn influence collective migration [35]. Capturing such effects, therefore, requires a theoretical description that resolves run-and-tumble dynamics and transport in higher dimensions.

Taken together, existing theoretical approaches capture complementary aspects of aerotactic behavior but do not provide a unified explanation for density-dependent migration in self-generated oxygen gradients. The experimentally observed migration reversal therefore calls for a new framework that explicitly accounts for the coupled dynamics of bacterial motion, oxygen transport, and consumption.

III. KINETIC THEORY

A. Model

The reversal in migration direction indicates a feedback between bacterial accumulation and oxygen depletion, arising from the tendency of *E. coli* to accumulate at an intermediate oxygen concentration [36]. To capture this feedback, we formulate a two-dimensional (2D) kinetic theory [26,37–39] for run-and-tumble bacteria in a self-generated oxygen gradient.

In this framework, the bacterial population is described by a probability density function $\psi(\mathbf{x}, \theta, t)$ that

characterizes the probability of finding a bacterium at $\mathbf{x} = (x, y)$ with orientation $\mathbf{p} = (\cos\theta, \sin\theta)$ at time t. $\psi(\mathbf{x}, \theta, t)$ satisfies a conservation equation,

$$\partial_t \psi + \nabla_{\mathbf{x}} \cdot (\dot{\mathbf{x}}\psi) = d_r \partial_\theta^2 \psi - \Lambda(\mathbf{x}, \theta)\psi + \int_0^{2\pi} \Lambda(\mathbf{x}, \theta')K(\theta|\theta')\psi(\mathbf{x}, \theta')\mathrm{d}\theta', \quad (1)$$

where $\dot{\mathbf{x}} = V_0\mathbf{p} - d_T \nabla_{\mathbf{x}} \ln\psi$ is the translational flux, with bacterial swimming speed V_0 and translational diffusivity d_T. The right-hand side of Eq. (1) captures the rotational diffusion with a diffusivity d_r and the run-and-tumble reorientation of bacteria. The tumbling rate $\Lambda(\mathbf{x}, \theta)$ depends on position and orientation; $-\Lambda\psi$ represents loss from direction θ, while the integral accounts for reorientation into θ from θ'. We assume isotropic, uncorrelated tumbles with transition probability $K(\theta|\theta') = 1/(2\pi)$.

As oxygen diffuses along $x \in [0, L]$ from the air-water interface at $x = 0$, bacterial density varies only with x. Thus, Eq. (1) simplifies to

$$\partial_t \psi + \partial_x(V_0 \cos\theta\psi) = d_T \partial_x^2 \psi + d_r \partial_\theta^2 \psi - \Lambda(x, \theta)\psi + \frac{1}{2\pi}\int_0^{2\pi} \Lambda(x, \theta')\psi(x, \theta')\mathrm{d}\theta'. \quad (2)$$

No-flux boundaries are enforced to ensure the conservation of total bacterial number,

$$V_0 \cos\theta\psi = d_T \partial_x \psi \quad \text{at } x = 0, L. \quad (3)$$

The local density $\rho(x, t) = \int_0^{2\pi} \psi(x, \theta, t)d\theta$ is normalized so that $1/L \int_0^L \rho(x, t)dx = \rho_0$.

To model the tendency of *E. coli* to accumulate at an intermediate oxygen concentration $c = [c_{\min}, c_{\max}]$ optimal for metabolism [36,40], we extend the model of Mazzag *et al.* [34]. The tumbling frequency $\Lambda(x, \theta)$ is given as

$$\Lambda(x, \theta) = \begin{cases} \Lambda_0 \exp(-\zeta \cos\theta), & \text{for } c > c_{\max} \text{ and } \cos\theta > 0, \\ \Lambda_0, & \text{for } c_{\min} \leqslant c \leqslant c_{\max}, \\ \Lambda_0 \exp(+\zeta \cos\theta), & \text{for } c < c_{\min} \text{ and } \cos\theta < 0, \end{cases} \quad (4)$$

where Λ_0 is the baseline tumbling rate and $\zeta > 0$ quantifies the sensitivity of tumbling frequency to oxygen concentration. Outside a sensing window $[c_{\mathrm{lb}}, c_{\mathrm{ub}}]$, we assume $\Lambda = \Lambda_0$.

Finally, the variation of oxygen concentration via diffusion and consumption is described by

$$\partial_t c = D_O \partial_x^2 c - \kappa(c)\rho, \quad (5)$$

where D_O is the diffusivity of oxygen in water and $\kappa(c)$ is the consumption rate of oxygen by bacteria given as [28,34,41]

$$\kappa(c) = \begin{cases} \kappa_0, & c > 0, \\ 0, & c = 0. \end{cases} \quad (6)$$

The oxygen concentration at the air-water interface is fixed at the saturation concentration $c(0) = c_0$, whereas at the interior end of the channel, we prescribe a no-flux boundary condition, $\partial_x c(L) = 0$.

We use parameter values extracted from prior experiments. Specifically, the baseline tumbling frequency is $\Lambda_0 = 1\,\mathrm{s}^{-1}$ and swimming speed is $V_0 = 20\,\mu\mathrm{m/s}$. Translational and rotational diffusivities are $d_T = 4 \times 10^{-10}\,\mathrm{m}^2/\mathrm{s}$ and $d_r = 0.05\,\mathrm{s}^{-1}$, respectively [26]. The oxygen saturation at the interface is $c_0 = 180\,\mu\mathrm{M}$ [42], with sensing thresholds $c_{\mathrm{ub}} = 0.9c_0$, $c_{\max} = 0.1c_0$, $c_{\min} = 0.05c_0$, and $c_{\mathrm{lb}} = 5 \times 10^{-5}c_0$ [40,43]. We set the sensitivity $\zeta = 0.8$, which yields run lengths consistent with experiments. Oxygen diffusivity and consumption rate are $D_O = 2.4 \times 10^3\,\mu\mathrm{m}^2/\mathrm{s}$ and $\kappa_0 = 1.2 \times 10^{-9}\,\mu\mathrm{M}/(\mathrm{cells/ml\,s})$ [41]. The qualitative dynamics shown below remain robust over physiologically relevant ranges.

We solve Eqs. (2) and (5) using the open source spectral solver Dedalus [44] with a domain size $L = 1200\,\mu\mathrm{m}$ at different values of overall density ρ_0. Following the experiments, the initial density of bacteria, $\rho = \rho_0$, is spatially uniform, and the initial oxygen concentration in the channel is $c = 0$.

B. Results

The kinetic theory captures the key features observed in the experiments. Figure 3 shows the temporal evolution of $\rho(x)$ for three representative values of ρ_0. Across all densities, bacteria rapidly form a high-density peak. As in experiments, the peak forms closer to the interface at higher ρ_0 and shifts over time in a density-dependent manner. For low density ($\rho_0 = 1 \times 10^9$ cells/ml), the peak migrates away from the interface [Fig. 3(a)], while at high density ($\rho_0 = 4 \times 10^9$ cells/ml), it moves toward the interface [Fig. 3(c)]. At intermediate density ($\rho_0 = 1.5 \times 10^9$ cells/ml), the peak remains nearly stationary [Fig. 3(b)].

Using the same procedure as in experiments, we compute the average migration velocity $v_m(\rho_0)$ from the kinetic theory [Fig. 2(b); details are provided in Appendix E 2]. Without free parameters, the predicted speed is within a factor of 3 of experimental values. We defer the discussion regarding the possible origins of this quantitative mismatch to Sec. V. More importantly, the model correctly captures the critical density ρ_c and the trend of v_m. This agreement suggests density-dependent feedback between bacterial accumulation and oxygen consumption as the mechanism reconciling long-standing conflicting reports of *E. coli* aerotaxis [8,27,28].

IV. PHYSICAL MODEL

The kinetic theory captures the reversal of bacterial migration with density and points to a feedback mechanism between oxygen diffusion/consumption and aerotactic accumulation. To pinpoint the essential physical ingredients underlying this feedback, we construct a simplified one-dimensional model. This physical model is informed by two key insights gained from the kinetic theory: (a) fast oxygen diffusion and consumption that establish a quasisteady oxygen profile, and (b) slow aerotaxis that redistributes bacteria within the channel. The separation of the timescales of these two processes allows us to treat the oxygen field as quasistatic relative to the bacterial motion. We discuss the physics of the two processes below.

A. Short-time oxygen diffusion and consumption

We first consider the diffusion of oxygen into a suspension of uniform bacterial density in the absence of migration. The

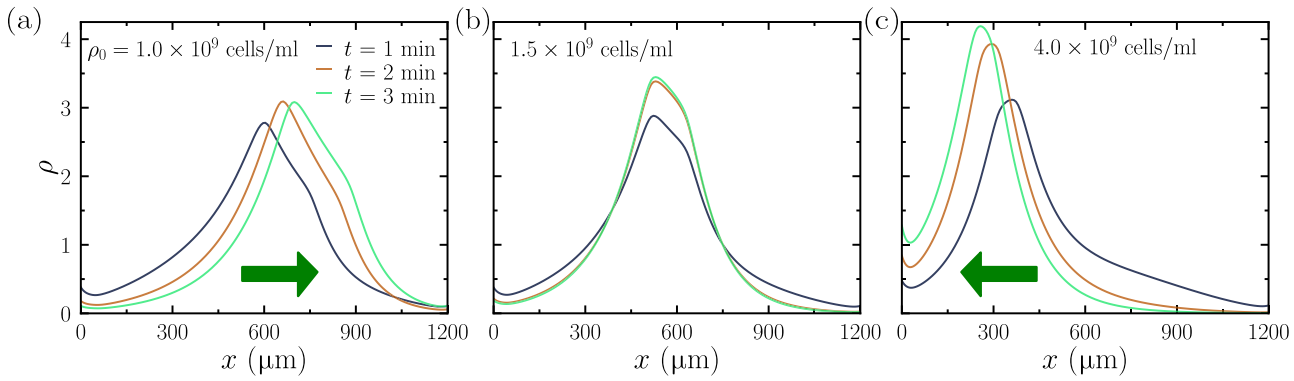

FIG. 3. Bacterial aerotaxis from kinetic theory. Temporal variation of bacterial density profiles for $\rho_0 = 1.0 \times 10^9$ cells/ml [panel (a)], 1.5×10^9 cells/ml [panel (b)], and 4×10^9 cells/ml [panel (c)]. The migration directions of the bacterial population in panels (a) and (c) are shown using the green arrows.

steady-state oxygen profile satisfies

$$D_O \partial_x^2 c = \kappa(c)\rho_0, \tag{7}$$

with $c(0) = c_0$ and $\partial_x c(L) = 0$. By positing that the oxygen is depleted at a finite penetration depth ℓ_p (see Appendix F 1 for details), this yields

$$\ell_p = \sqrt{\frac{2D_O c_0}{\kappa_0 \rho_0}}, \quad \text{where} \quad c(\ell_p) = 0. \tag{8}$$

The characteristic time for oxygen diffusion over this length, $\tau_1 \approx \ell_p^2/D_O$, is much shorter than the aerotactic migration time $\tau_2 \approx \ell_p/v_c$, where v_c is the characteristic migration speed of aerotactic bacteria. Using $\rho_c = 1.5 \times 10^9$ cells/ml and a representative $v_c \simeq 0.3\,\mu$m/s from experiments gives $\tau_2/\tau_1 = D_O/(\ell_p v_c) \approx 12$, confirming that oxygen profiles relax rapidly to a quasisteady profile long before noticeable bacterial migration. The initial peak position then follows from $c(x_p^0) = c^*$,

$$x_p^0 = \sqrt{\frac{2D_O}{\kappa_0 \rho_0}}(\sqrt{c_0} - \sqrt{c^*}), \tag{9}$$

which predicts $x_p^0 \sim \sqrt{1/\rho_0}$, consistent with both experiments and kinetic theory. Here, c^* is taken to be the mean of the preferred range of oxygen concentration [Eq. (4)], $c^* \equiv (c_{\max} + c_{\min})/2$. Equation (9) agrees well with the kinetic theory (Fig. 4 inset), indicating that early band formation is governed by oxygen diffusion and consumption, and highlighting the timescale separation as a key feature of the dynamics. The separation of timescales becomes less apparent at low ρ_0 because ℓ_p increases as ρ_0 decreases [Eq. (8)], leading to the deviation between predictions and simulations at low ρ_0 in the inset of Fig. 4. To connect this separation to the observed reversal, we next analyze the long-term behavior of bacterial aerotaxis.

B. Long-time bacterial aerotaxis

On the slower timescale of bacterial migration, we describe the bacterial population with a 1D advection-diffusion equation in which the drift velocity is set by the reversal rates for cells swimming along $\pm x$. Denoting $\lambda^+(c)$ and $\lambda^-(c)$ as the reversal rates for right- and left-moving cells, respectively, we define their average $\bar{\lambda} \equiv (\lambda^+ + \lambda^-)/2$ and mismatch $\Delta\lambda(c) \equiv \lambda^-(c) - \lambda^+(c)$. The population density then evolves according to an advection-diffusion equation (derived in Appendix F 2),

$$\frac{\partial \rho}{\partial t} = -\frac{V_0 \Delta\lambda}{2\bar{\lambda}} \frac{\partial \rho}{\partial x} + \frac{V_0^2}{2\bar{\lambda}} \frac{\partial^2 \rho}{\partial x^2}, \tag{10}$$

where the first term represents directed migration arising from a bias in tumbling and the second term represents effective diffusion due to random reorientations. The local drift velocity $v_b \equiv V_0 \Delta\lambda/(2\bar{\lambda})$ depends on the oxygen concentration through $\Delta\lambda[c(x)]$.

At steady state, the bacterial and oxygen fields are coupled via

$$V_0 \frac{d\rho}{dx} = \Delta\lambda[c(x)]\rho(x), \tag{11}$$

$$\frac{d^2 c}{dx^2} = \frac{\kappa(c)}{D_O}\rho(x), \tag{12}$$

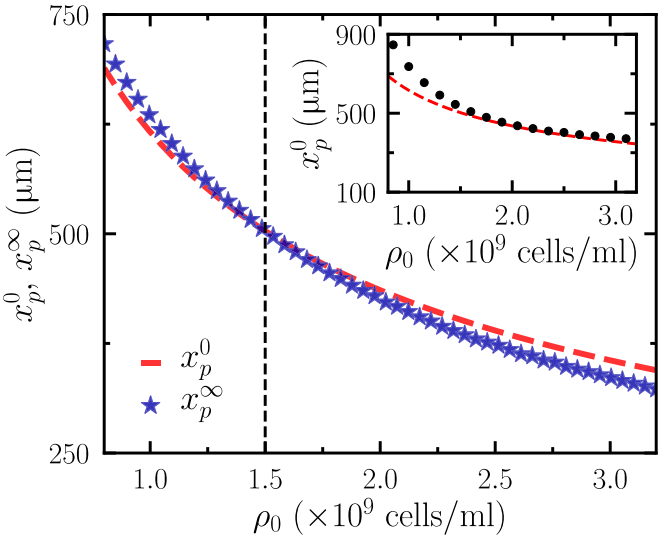

FIG. 4. Initial peak position, x_p^0, and the steady-state peak position, x_p^∞, as a function of overall bacterial density ρ_0. The dashed line indicates the critical density where $x_p^0 = x_p^\infty$. Inset: Initial peak positions x_p^0 vs ρ_0. The line shows the prediction of Eq. (9), while symbols are the average x_p^0 over a 20-s interval centered around τ_1 from the kinetic theory.

which are again subject to the conservation of bacterial number $1/L\int_0^L \rho(x)dx = \rho_0$ and the boundary conditions of oxygen concentration $c(0) = c_0$ and $\partial_x c(L) = 0$. Integrating Eq. (11) gives the steady-state bacterial density profile

$$\rho(x) \propto \exp\left(\int_0^x \Delta\lambda[c(x')]dx'/V_0\right), \tag{13}$$

whose maximum defines the steady-state peak position x_p^∞.

A stable density peak forms only if the tumbling bias $\Delta\lambda$ changes sign at the preferred oxygen concentration c^*, causing bacteria on either side of c^* to move toward this concentration [34]. We describe this behavior phenomenologically as $\Delta\lambda = \alpha\tanh[\gamma(c - c^*)]$, where α represents the magnitude of the bias and γ controls the sharpness of the sign change. α sets the typical migration speed $v_b = V_0\Delta\lambda/(2\bar{\lambda}) \approx 0.3\,\mu\text{m/s}$ and is therefore fixed at $\alpha = 0.03\,\text{s}^{-1}$. We further choose $\gamma = 0.33\,\mu\text{M}^{-1}$, although the critical density ρ_c predicted below is largely insensitive to variations in γ over several orders of magnitude (Appendix F 3). The steady-state peak position x_p^∞ then follows from the density profile $\rho(x)$ computed using this form of $\Delta\lambda$.

Comparing the initial and steady-state peak positions, x_p^0 and x_p^∞, reveals an intersection at a critical density $\rho_c \approx 1.5 \times 10^9$ cells/ml (Fig. 4), in excellent agreement with both experiments and kinetic theory. This intersection marks the density at which the migration direction reverses, with the bacterial band moving toward the interface for $x_p^0 > x_p^\infty$ and away from it for $x_p^0 < x_p^\infty$. Together, the separation of oxygen and bacterial timescales and the sign change of $\Delta\lambda$ at c^* constitute the minimal physical ingredients underlying the observed density-dependent reversal of the bacterial band, illustrating how feedback between oxygen diffusion/consumption and aerotaxis can invert the direction of collective migration.

V. DISCUSSION

Our results demonstrate that the direction of collective migration in *E. coli* aerotaxis is governed by population density through feedback between oxygen consumption and diffusion and taxis toward a preferred oxygen concentration. The reversal of migration arises from the competition between oxygen penetration and bacterial accumulation, whose characteristic length scales determine the prevailing direction of collective movement. At a critical density, the balance of these processes stalls migration altogether, marking a transition between two different collective states. This framework resolves long-standing contradictions in bacterial aerotaxis and highlights how the coupling between metabolism and movement can transform the collective dynamics of living active matter.

The ingredients underlying the migration reversal, namely, biased motion toward a preferred oxygen concentration together with oxygen diffusion and consumption also appear in more elaborate form in the model of Mazzag *et al.* [34]. However, these authors focused on the formation and positioning of aerotactic bands and did not consider the direction of collective migration. In particular, the work did not examine whether varying bacterial density alone, under otherwise fixed environmental conditions, could produce the reversal of bacterial collective migration. Determining whether such a transition arises within that framework would require a dedicated analysis of the model and therefore lies beyond the scope of the present study.

More importantly, the kinetic theory formulated here yields steady-state predictions that differ qualitatively from those of the reduced one-dimensional description of Ref. [34]. In this one-dimensional description, the aerotactic band corresponds to a steady state with zero net polarity at all positions, i.e., a local balance between bacteria swimming up and down the oxygen gradient. In contrast, our kinetic theory predicts a steady state with a finite net polarity that persists at long times, reflecting a persistent imbalance between bacteria swimming toward and away from the preferred oxygen concentration. As a result, the steady state is not characterized by complete orientational symmetry but instead retains directional structure that depends on bacterial density and transport dynamics. Such a crucial difference stems from the explicit treatment of orientational dynamics and bacterial transport—particularly run-and-tumble reorientation and translational diffusion—in the kinetic framework, which cannot be captured in a reduced one-dimensional description. Consequently, the kinetic theory not only captures population-level migration but also yields predictions for single-cell statistics within the band, which may be accessible in future experiments tracking individual bacterial trajectories.

Although our kinetic theory, parametrized using experimentally measured values for *E. coli*, correctly captures the critical density ρ_c, it does not reproduce the measured migration velocity v_m quantitatively. This discrepancy likely reflects the simplified nature of the present framework, which is designed to identify the mechanism of density-controlled migration reversal rather than to provide a complete quantitative description of aerotaxis. In particular, the oxygen-dependent tumble response is modeled through a phenomenological extension of the form introduced by Mazzag *et al.* [34], which is likely only an approximate description of the true run-and-tumble dynamics of *E. coli*. Direct measurements of single-cell trajectories under controlled oxygen conditions would therefore provide an important experimental input for refining the model. More generally, the molecular mechanism linking external oxygen to changes in tumbling dynamics is only partially understood [40], limiting the construction of a more quantitatively predictive theory. In addition, the present model is two dimensional, whereas bacterial motion in the experiments is intrinsically three dimensional. Extending the framework to three dimensions, together with a more precise experimental characterization of oxygen-dependent tumbling and swimming speed, should help improve the quantitative prediction of v_m.

As facultative anaerobes, *E. coli* inhabit the mucosal surface of the mammalian intestine [45], where oxygen concentrations are only a few percent of the atmospheric levels [46]—closely matching the optimal range identified in our study. The critical density ρ_c, around 1×10^9 cells/ml, also coincides with the native population density of intestinal *E. coli* [47], at which collective migration arrests and cells may transition from motile to sessile behavior, promoting surface colonization and biofilm formation. These observations

suggest that the optimal oxygen level and the critical density identified here mirror the native conditions of *E. coli* in the mammalian intestine, hinting that the collective migration dynamics revealed in our experiments may reflect an adaptation to the oxygen landscape of the bacterial natural habitat.

More broadly, our findings connect to a substantial body of work on collective migration along self-generated chemical gradients, which has been studied experimentally and theoretically in both bacterial and eukaryotic chemotaxis [48–53]. In these systems, cells actively reshape their chemical environment through consumption or secretion, generating gradients that in turn guide collective motion. Similar feedback between metabolism, movement, and environment also underlies a range of self-organization processes in biology, including migration guided by self-generated stiffness gradients [54], aggregation driven by resource consumption in photosynthetic microbes [55], and thermoregulatory clustering in animal groups [56–58]. Within this broader context, our work highlights how bacterial density can act as a key control parameter for collective migration in systems with self-generated gradients, through feedback between population dynamics and environmental modification.

ACKNOWLEDGMENTS

We thank Gladys Alexandre, Vasilios Alexiades, Satyam Anand, Alex Mogilner, Yuhai Tu, and Tingtao Zhou for insightful discussions. D.G. and X.C. were supported by NSF CBET 2028652 and 2400584 and the David and Lucile Packard Foundation. B.C. acknowledges the support of the Department of Atomic Energy, Government of India, under Project no. RTI4019. We acknowledge the Minnesota Supercomputing Institute (MSI) at the University of Minnesota for providing resources that contributed to the research results reported within this paper.

DATA AVAILABILITY

The data underlying all figures of this paper and the Python script used to solve the kinetic theory equations are openly available [59].

APPENDIX A: CELL CULTURE

We prepared bacterial suspensions containing a mixture of fluorescently tagged and nonfluorescent wild-type *E. coli* strain AW HCB1732. The wild-type cells were tagged with green fluorescent protein (GFP) by inserting the plasmid pJUMP27-1A(sfGFP) (Addgene #126974). The bacterial suspensions were cultured by inoculating a small quantity of frozen stock in 2 ml Terrific Broth (TB) [tryptone 1.2% (w/v), yeast extract 2.4% (w/v), and glycerol 0.4% (w/v)]. The cell culture for the GFP-tagged cells was supplemented with 0.1% (v/v) of 50 mg/ml kanamycin. These cultures were then incubated in an orbital shaker at 250 rpm at 37 °C for 12 to 16 h in the late exponential phase. To ensure the motility of the cells, the bacterial suspensions were then diluted 1:100 with fresh TB and grown in the exponential phase for 6.5 h in the orbital shaker at 30 °C.

At the end of the growth phases of cells, we mixed the liquid cultures containing the fluorescent and nonfluorescent strains of the bacteria. The volume of the two cultures for mixing was adjusted depending on the total concentration of cells. For each overall concentration, we ensured that the number of fluorescent cells in the field of view was optimized to have a sufficient number of cells for statistical averaging while allowing for the individual cell trajectories to be tracked without overlap from their neighbors. The motile cells were then harvested using gentle centrifugation at 800*g* for 5 min, followed by discarding the supernatant TB, and resuspending the cells in motility buffer [0.01 M potassium phosphate, 0.067 M NaCl, and 10^{-4} M EDTA, pH 7.0]. The suspension was then washed twice and the desired overall concentration of cells was obtained by adding motility buffer. The overall density of the bacterial suspension containing fluorescent and nonfluorescent cells in the motility buffer was measured using a biophotometer via optical density at 600 nm (OD_{600}). We collected bacterial suspensions of different densities ranging from 6×10^8 to 8×10^9 cells/ml.

APPENDIX B: EXPERIMENTAL SETUP AND IMAGING

We used a glass capillary channel (Rectangle-Miniature Hollow Glass Tubing 5010, VitroTubes^{TM}) with a wall thickness of 0.07 mm, a vertical height of 100 μm, and a horizontal width of 1.0 mm. The original channel is 50 mm in length, from which we cut a section with a length of 25 mm. Using UV-curable adhesive, we then attached this capillary tube to a microscope cover glass of $24 \times 60\,\text{mm}^2$. We filled the channel with a bacterial suspension and sealed one end with the adhesive, leaving the other end open for oxygen to diffuse into the channel. To minimize evaporation during the experiment, we covered the channel with an acrylic lid and placed soaked cotton wicks inside the chamber. The thin walls of the capillary channel allowed high-magnification imaging of individual bacteria [Fig. 1(b)].

The capillary channel filled with the bacterial suspension was mounted on a piezo stage with horizontal motion controlled using the Nikon NIS-Elements macro language. Bacteria in the channel were imaged using a Nikon Plan APO 60× oil objective (NA = 1.4) on an inverted Nikon Ti-Eclipse microscope with a Yokogawa CSU-X confocal spinning disk. The sample was excited using a 488-nm laser.

The field of view of our imaging is $160 \times 120\,\mu\text{m}^2$. We wrote a custom macro script, allowing us to image swimming bacteria in the field of view for 10 s at 30 frames/s and then shift by 120 μm to image an immediately adjacent region. We started imaging from the air-water interface at $x = 0$ and shifted the lens horizontally to image progressively deeper into the capillary channel. We imaged at 10 consecutive horizontal locations along the channel covering a total length of 1200 μm. The entire scanning along the length of the channel, including the time taken to write video files on disk, took approximately 2 min. After waiting an additional 2 min, we scanned the channel again to obtain the spatial information at the next time instant. The combined duration of the channel scan and waiting time allowed data recording at 4-min intervals, with timestamps at $t = 4$, 8, 12, 16, and 20 min, and beyond for low-density experiments. The duration

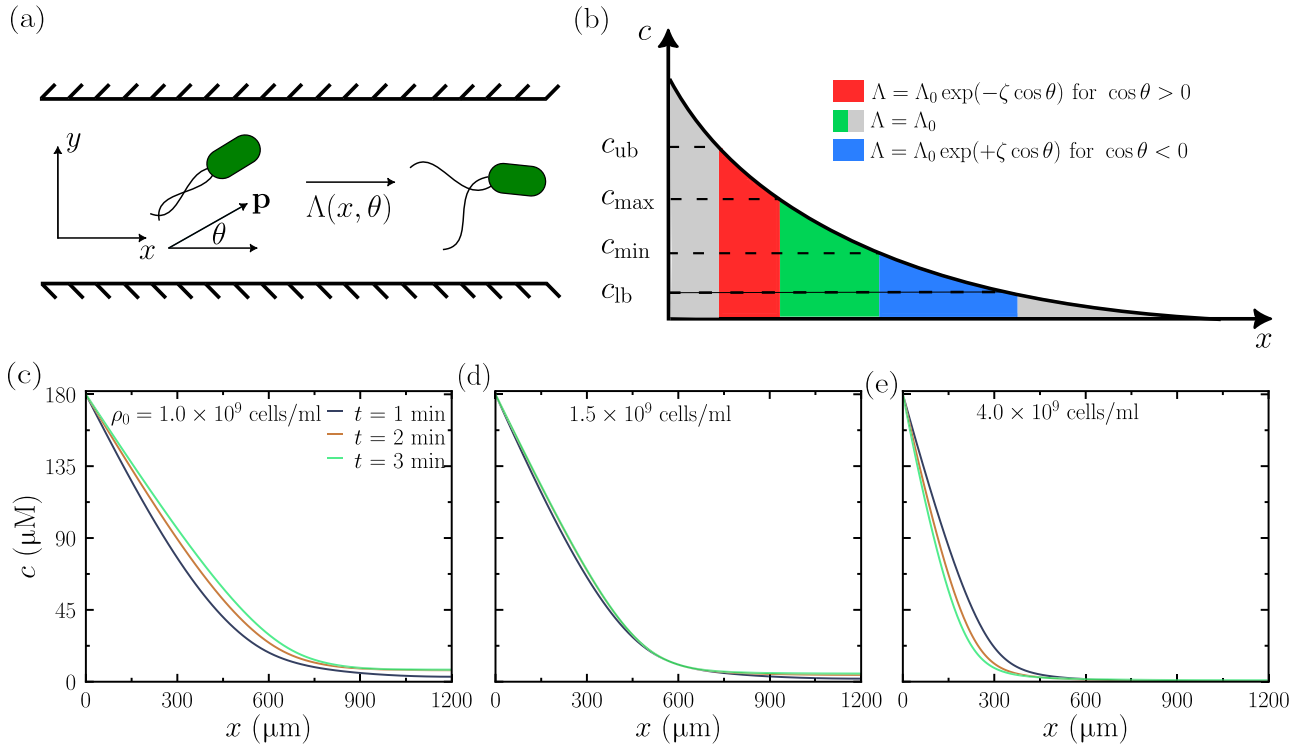

FIG. 5. Kinetic theory. (a) Schematic of the run-and-tumble of bacteria in a 2D channel. (b) Schematic illustrating variations in tumbling frequency Λ at different oxygen concentrations $c(x)$ (not to scale). Temporal variation of oxygen concentration profiles for $\rho_0 = 1.0 \times 10^9$ cells/ml [panel (c)], 1.5×10^9 cells/ml [panel (d)], and 4×10^9 cells/ml [panel (e)].

of our observation was shorter than the division time of the bacteria, ensuring that the effects of growth and division can be neglected. We imaged the samples $25-30\,\mu$m above the bottom wall of the capillary channel to avoid the influence of the boundary.

APPENDIX C: IMAGE ANALYSIS AND BACTERIAL DENSITY PROFILE

The image stacks from confocal microscopy were processed using the Python library skimage. The GFP-tagged cells appeared as bright ellipsoids against a dark background [Fig. 1(b)]. We binarized the video frames using the Niblack algorithm [60] and obtained the centroid positions of the cells. For a given time step of a scan along the channel, we recorded the spatial coordinate of each fluorescently tagged bacterium detected over the scanning duration. The total length of the observed channel of $1200\,\mu$m was binned into $60\,\mu$m windows and the number of bacteria at each of the $n_w = 1200/60 = 20$ windows, $n(x_i)$, was calculated. To reduce noise from fluctuations in the observed bacterial count, we applied a Savitzky-Golay filter, fitting a fifth-order polynomial with a window size of 9, which yielded the spatially smoothed bacterial count, $n_s(x)$. Finally, the normalized local density of bacteria was calculated as $\rho(x) = n_s(x)/(N_s/n_w)$, where $N_s = \Sigma_{i=1}^{n_w} n_s(x_i)$ is the total number of bacteria observed along the length of the channel obtained after spatial smoothing (Fig. 1). The normalized density eliminated the influence of the variation of the ratio of the fluorescent to nonfluorescent bacteria for different overall bacterial densities.

APPENDIX D: MIGRATION VELOCITY OF BACTERIAL POPULATION

To obtain the population migration velocity in experiments, v_m, we first calculated the mean position of the bacterial population $\bar{x}(t) = \sum_{i=1}^{n_w} x_i \rho(x_i, t) / \sum_{i=1}^{n_w} \rho(x_i, t)$. For each experiment, v_m was obtained through a linear fit of $\bar{x}(t)$ versus t. For each bacterial density ρ_0, the experiment was repeated three times independently, and the reported value of v_m is the mean across experiments. Error bars shown in Fig. 2 correspond to the standard error of the mean across independent experiments.

APPENDIX E: KINETIC THEORY

1. Tumbling rate $\Lambda(x, \theta)$ and oxygen concentration profile $c(x)$

Figure 5(a) shows a schematic of the run-and-tumble dynamics of the bacterial population in 2D, where the probability density function $\psi(\mathbf{x}, \theta, t)$ is specified over positions $\mathbf{x} = (x, y)$ and orientations $\mathbf{p} = (\cos\theta, \sin\theta)$ at time t. Figure 5(b) shows a schematic depicting the variation of tumbling rate Λ along a typical oxygen concentration profile, as described by Eq. (4). Finally, Figs. 5(c)–5(e) show the spatiotemporal evolution of the oxygen concentration, $c(x, t)$, for the three different bacterial densities, corresponding to the three examples shown in Figs. 3(a)–3(c), respectively.

2. Migration velocity of bacterial population

To evaluate the population migration velocity from the kinetic theory, we first obtained the mean position of the

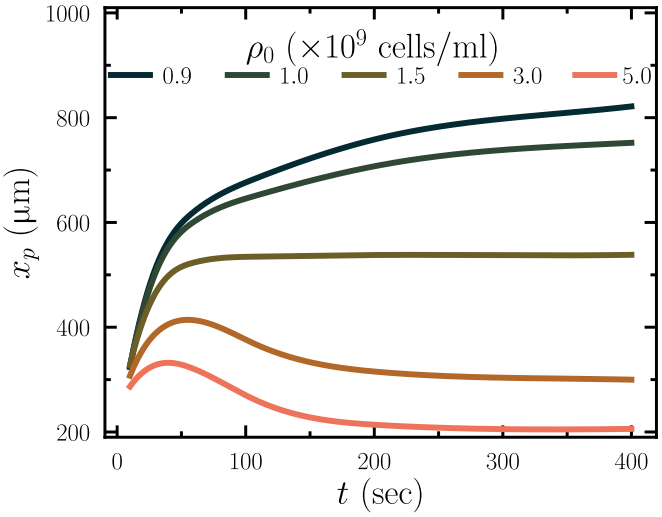

FIG. 6. Temporal evolution of bacterial density peak x_p at different overall cell densities ρ_0 predicted by kinetic theory.

bacterial population using $\bar{x}(t)=\int_0^L x\rho(x,t)\mathrm{d}x/\int_0^L \rho(x,t)\mathrm{d}x$. The instantaneous velocity was then obtained as $v(t)=\bar{x}'(t)$. The average population migration velocity was calculated following $v_m=\int_{t_1}^{t_2} v(t)\mathrm{d}t/(t_2-t_1)$ over a time interval $[t_1,t_2]$. The lower time limit t_1 was chosen to exclude the influence of the transient dynamics at short times. For $\rho<\rho_c$, the bacterial density peak shows unidirectional migration away from the interface (Fig. 6). In this low-density regime, we chose the inflection point of $\bar{x}(t)$ as t_1, i.e., $\bar{x}''(t_1)=0$. For $\rho>\rho_c$, the peak of the density profile x_p is nonmonotonic at early times (Fig. 6). Here, we chose t_1 as the time where x_p reaches its maximum, i.e., $x_p'(t_1)=0$ and $x_p''(t_1)<0$. For both cases, the upper time limit t_2 was chosen such that $\bar{x}(t)$ has reached steady state with $v(t>t_2)<10^{-4}$ μm/s.

APPENDIX F: PHYSICAL MODEL

1. Short-time oxygen diffusion and consumption

Our experiments and simulations reveal that the aerotactic response of bacteria occurs much more slowly than the diffusion and consumption of oxygen in the capillary channel. To illustrate this separation of timescales, we estimate the penetration depth of oxygen $x=\ell_p$, at which oxygen runs out due to the consumption of uniformly distributed bacteria. Solving Eq. (7) subject to $c(0)=c_0$ and $\partial_x c(L)=0$, and positing that the oxygen concentration falls to zero at $x=\ell_p\leqslant L$, $c(x)$ takes the form

$$c(x)=\begin{cases} c_0+\frac{\kappa_0\rho_0}{2D_O}(x^2-2\ell_p x), & x\leqslant \ell_p,\\ 0, & x\geqslant \ell_p. \end{cases} \tag{F1}$$

The condition $c(\ell_p)=0$ then yields the penetration depth given in Eq. (8).

2. Long-time bacterial aerotaxis

We estimate the steady-state bacterial density profile at long time. To this end, we consider a 1D telegrapher's equation model for the bacteria population and define two subpopulations of bacteria moving along the $+x$ and $-x$ directions with probability densities P^+ and P^-, respectively. Their evolution obeys

$$\frac{\partial P^+}{\partial t}=-V_0\frac{\partial P^+}{\partial x}+[-\lambda^+P^++\lambda^-P^-], \tag{F2}$$

$$\frac{\partial P^-}{\partial t}=+V_0\frac{\partial P^-}{\partial x}-[-\lambda^+P^++\lambda^-P^-], \tag{F3}$$

where λ^+ (λ^-) is the rate at which a bacterium moving along the $+x$ ($-x$) direction reverses its swimming direction, capturing the run-and-tumble dynamics of *E. coli*. These transport equations are complemented by the no-flux boundary conditions $P^+(0)=P^-(0)$ and $P^+(L)=P^-(L)$ that ensure conservation of total number of bacteria. Adding and subtracting Eqs. (F2) and (F3), we obtain

$$\frac{\partial\rho}{\partial t}=-V_0\frac{\partial\delta}{\partial x} \tag{F4}$$

and

$$\frac{\partial\delta}{\partial t}=-V_0\frac{\partial\rho}{\partial x}-2\bar{\lambda}\delta+\Delta\lambda\rho, \tag{F5}$$

where $\rho=P^++P^-$ is the local density of bacteria, $\delta=P^+-P^-$ is the local density difference of the two subpopulations, $\bar{\lambda}=(\lambda^++\lambda^-)/2$ is the local average reversal frequency, and $\Delta\lambda=\lambda^--\lambda^+$ is the mismatch between the reversal frequencies of the left- and right-going subpopulations.

Assuming that the density difference δ equilibrates faster compared to the density ρ [61–63], a quasistatic approximation of $\partial_t\delta\approx 0$ gives $\delta=(-V_0\partial_x\rho+\Delta\lambda\rho)/2\bar{\lambda}$ from Eq. (F5). Substituting δ in Eq. (F4) recovers the advection-diffusion equation [Eq. (10)], where $v_b\equiv V_0\Delta\lambda/2\bar{\lambda}$ is the migration speed of aerotactic bacteria. At steady state, this reduces to Eq. (11), which is subject to the conservation of bacterial number $\int_0^L\rho(x)dx=L\rho_0$.

TABLE I. ρ_c (in 10^9 cells/ml) as a function of α (s^{-1}) and γ ($\mu\mathrm{M}^{-1}$). "–" indicates that the migration direction of the density peak does not reverse in the 1200-μm-long channel.

α \ γ	0.003	0.005	0.05	0.55	5.55
0.07	–	0.6	0.8	–	–
0.06	–	0.6	1.3	0.5	0.5
0.04	–	0.4	2.5	1.0	1.0
0.02	–	–	0.5	3.0	3.0
0.01	–	–	–	–	8.0

3. Effect of varying α and γ

We examined how the critical bacterial density ρ_c depends on the parameters α and γ in the expression $\Delta\lambda=\alpha\tanh[\gamma(c-c^*)]$ in our physical model. Here, α sets the magnitude of $\Delta\lambda$, while γ controls the steepness of the variation of $\Delta\lambda$ near $c=c^*$. We focused on the regime where the crossover between the initial peak position, x_p^0, and the final peak position, x_p^∞, occurs within the experimental domain of $0<x<1200$ μm. We found that varying $0.02\,\mathrm{s}^{-1}<\alpha<0.06\,\mathrm{s}^{-1}$ and $0.05\,\mu\mathrm{M}^{-1}<\gamma<5.55\,\mu\mathrm{M}^{-1}$ leads to ρ_c generally agreeing with our experimental observation (Table I).

[1] S. C. Takatori, T. Quah, and J. B. Rawlings, Feedback control of active matter, Annu. Rev. Condens. Matter Phys. **16**, 319 (2025).

[2] A. Gelimson, K. Zhao, C. K. Lee, W. T. Kranz, G. C. L. Wong, and R. Golestanian, Multicellular self-organization of *P. aeruginosa* due to interactions with secreted trails, Phys. Rev. Lett. **117**, 178102 (2016).

[3] F. L. Memarian, J. D. Lopes, F. J. Schwarzendahl, M. G. Athani, N. Sarpangala, A. Gopinathan, D. A. Beller, K. Dasbiswas, and L. S. Hirst, Active nematic order and dynamic lane formation of microtubules driven by membrane-bound diffusing motors, Proc. Natl. Acad. Sci. USA **118**, e2117107118 (2021).

[4] R. M. Adar and J.-F. Joanny, Environment-stored memory in active nematics and extra-cellular matrix remodeling, Phys. Rev. Lett. **133**, 118402 (2024).

[5] G. H. Wadhams and J. P. Armitage, Making sense of it all: Bacterial chemotaxis, Nat. Rev. Mol. Cell. Biol. **5**, 1024 (2004).

[6] V. Sourjik and N. S. Wingreen, Responding to chemical gradients: Bacterial chemotaxis, Curr. Opin. Cell Biol. **24**, 262 (2012).

[7] S. Park, P. M. Wolanin, E. A. Yuzbashyan, P. Silberzan, J. B. Stock, and R. H. Austin, Motion to form a quorum, Science **301**, 188 (2003).

[8] J. Adler, Chemotaxis in bacteria: Motile *Escherichia coli* migrate in bands that are influenced by oxygen and organic nutrients, Science **153**, 708 (1966).

[9] E. O. Budrene and H. C. Berg, Complex patterns formed by motile cells of *Escherichia coli*, Nature (London) **349**, 630 (1991).

[10] E. Lushi, R. E. Goldstein, and M. J. Shelley, Collective chemotactic dynamics in the presence of self-generated fluid flows, Phys. Rev. E **86**, 040902(R) (2012).

[11] T. W. Engelmann, Neue methode zur untersuchung der sauerstoffausscheidung pflanzlicher und thierischer organismen, Pflügers Archiv. **25**, 285 (1881).

[12] W. Pfeffer, Locomotorische richtungsbewegungen durch chemische reize, Untersuch. Botan. Inst. Tübingen **1**, 363 (1884).

[13] W. Pfeffer, Über chemotaktische bewegungen von bacterien, flagellaten und volvocineen, Untersuch. Botan. Inst. Tübingen **2**, 582 (1888).

[14] T. Fenchel, G. King, and T. Blackburn, *Bacterial Biogeochemistry: The Ecophysiology of Mineral Cycling*, 3rd ed. (Elsevier, Amsterdam, 2012).

[15] G. Gottschalk, *Bacterial Metabolism*, 2nd ed. (Springer, New York, 1986).

[16] D. Saintillan and M. J. Shelley, Theory of active suspensions, in *Complex Fluids in Biological Systems: Experiment, Theory, and Computation*, edited by S. E. Spagnolie (Springer, New York, 2015), pp. 319–355.

[17] I. S. Aranson, Bacterial active matter, Rep. Prog. Phys. **85**, 076601 (2022).

[18] F. Menolascina, R. Rusconi, V. I. Fernandez, S. Smriga, Z. Aminzare, E. D. Sontag, and R. Stocker, Logarithmic sensing in *Bacillus subtilis* aerotaxis, npj Syst. Biol. Appl. **3**, 16036 (2017).

[19] M. Adler, M. Erickstad, E. Gutierrez, and A. Groisman, Studies of bacterial aerotaxis in a microfluidic device, Lab Chip **12**, 4835 (2012).

[20] P. Prakash, Y. Baig, F. J. Peaudecerf, and R. E. Goldstein, Dynamics of an algae–bacteria microcosm: Photosynthesis, chemotaxis, and expulsion in inhomogeneous active matter, Proc. Natl. Acad. Sci. USA **122**, e2410225122 (2025).

[21] B. V. Hokmabad, A. Martínez-Calvo, S. Gonzalez La Corte, and S. S. Datta, Spatial self-organization of confined bacterial suspensions, Proc. Natl. Acad. Sci. USA **122**, e2503983122 (2025).

[22] I. Tuval, L. Cisneros, C. Dombrowski, C. W. Wolgemuth, J. O. Kessler, and R. E. Goldstein, Bacterial swimming and oxygen transport near contact lines, Proc. Natl. Acad. Sci. USA **102**, 2277 (2005).

[23] M. A. Bees, Advances in bioconvection, Annu. Rev. Fluid Mech. **52**, 449 (2020).

[24] C. Dombrowski, L. Cisneros, S. Chatkaew, R. E. Goldstein, and J. O. Kessler, Self-concentration and large-scale coherence in bacterial dynamics, Phys. Rev. Lett. **93**, 098103 (2004).

[25] A. Sokolov, R. E. Goldstein, F. I. Feldchtein, and I. S. Aranson, Enhanced mixing and spatial instability in concentrated bacterial suspensions, Phys. Rev. E **80**, 031903 (2009).

[26] B. Ezhilan, A. A. Pahlavan, and D. Saintillan, Chaotic dynamics and oxygen transport in thin films of aerotactic bacteria, Phys. Fluids **24**, 091701 (2012).

[27] M. Holz and S.-H. Chen, Spatio-temporal structure of migrating chemotactic band of *Escherichia coli*. I. Traveling band profile, Biophys. J. **26**, 243 (1979).

[28] C. Douarche, A. Buguin, H. Salman, and A. Libchaber, *E. coli* and oxygen: A motility transition, Phys. Rev. Lett. **102**, 198101 (2009).

[29] M. Eisenbach, A. Tamada, G. Omann, J. Segall, R. Firtel, R. Meili, D. Gutnick, M. Varon, J. W. Lengeler, and F. Murakami, *Chemotaxis* (World Scientific Publishing Company, Singapore, 2004).

[30] E. F. Keller and L. A. Segel, Traveling bands of chemotactic bacteria: A theoretical analysis, J. Theor. Biol. **30**, 235 (1971).

[31] I. R. Lapidus and R. Schiller, A model for traveling bands of chemotactic bacteria, Biophys. J. **22**, 1 (1978).

[32] D. Lauffenburger, C. R. Kennedy, and R. Aris, Traveling bands of chemotactic bacteria in the context of population growth, Bull. Math. Biol. **46**, 19 (1984).

[33] M. Schnitzer, S. Block, and H. Berg, Strategies for chemotaxis, in *Biology of the Chemotactic Response*, edited by J. P. Armitage and J. M. Lackie (Cambridge University Press, Cambridge, 1990), pp. 15–34.

[34] B. Mazzag, I. Zhulin, and A. Mogilner, Model of bacterial band formation in aerotaxis, Biophys. J. **85**, 3558 (2003).

[35] B. Ezhilan, R. Alonso-Matilla, and D. Saintillan, On the distribution and swim pressure of run-and-tumble particles in confinement, J. Fluid Mech. **781**, R4 (2015).

[36] A. Rebbapragada, M. S. Johnson, G. P. Harding, A. J. Zuccarelli, H. M. Fletcher, I. B. Zhulin, and B. L. Taylor, The Aer protein and the serine chemoreceptor Tsr independently sense intracellular energy levels and transduce oxygen, redox, and energy signals for *Escherichia coli* behavior, Proc. Natl. Acad. Sci. USA **94**, 10541 (1997).

[37] D. Saintillan and M. J. Shelley, Instabilities and pattern formation in active particle suspensions: Kinetic theory and continuum simulations, Phys. Rev. Lett. **100**, 178103 (2008).

[38] G. Subramanian and D. L. Koch, Critical bacterial concentration for the onset of collective swimming, J. Fluid Mech. **632**, 359 (2009).

[39] T. V. Kasyap and D. L. Koch, Chemotaxis driven instability of a confined bacterial suspension, Phys. Rev. Lett. **108**, 038101 (2012).

[40] B. L. Taylor, I. B. Zhulin, and M. S. Johnson, Aerotaxis and other energy-sensing behavior in bacteria, Annu. Rev. Microbiol. **53**, 103 (1999).

[41] X. Fu, S. Kato, J. Long, H. H. Mattingly, C. He, D. C. Vural, S. W. Zucker, and T. Emonet, Spatial self-organization resolves conflicts between individuality and collective migration, Nat. Commun. **9**, 2177 (2018).

[42] A. Al-Ani, D. Toms, D. Kondro, J. Thundathil, Y. Yu, and M. Ungrin, Oxygenation in cell culture: Critical parameters for reproducibility are routinely not reported, PLoS One **13**, e0204269 (2018).

[43] I. B. Zhulin, V. A. Bespalov, M. S. Johnson, and B. L. Taylor, Oxygen taxis and proton motive force in Azospirillum brasilense, J. Bacteriol. **178**, 5199 (1996).

[44] K. J. Burns, G. M. Vasil, J. S. Oishi, D. Lecoanet, and B. P. Brown, Dedalus: A flexible framework for numerical simulations with spectral methods, Phys. Rev. Res. **2**, 023068 (2020).

[45] T. Conway, K. A. Krogfelt, and P. S. Cohen, The life of commensal *Escherichia coli* in the mammalian intestine, EcoSal Plus **1**, 10 (2004).

[46] M. G. Espey, Role of oxygen gradients in shaping redox relationships between the human intestine and its microbiota, Free Radic. Biol. Med. **55**, 130 (2013).

[47] H. C. Berg, *E. coli in Motion* (Springer, New York, 2004).

[48] C. Scherber, A. J. Aranyosi, B. Kulemann, S. P. Thayer, M. Toner, O. Iliopoulos, and D. Irimia, Epithelial cell guidance by self-generated EGF gradients, Integr. Biol. **4**, 259 (2012).

[49] E. Donà, J. D. Barry, G. Valentin, C. Quirin, A. Khmelinskii, A. Kunze, S. Durdu, L. R. Newton, A. Fernandez-Minan, W. Huber, *et al.*, Directional tissue migration through a self-generated chemokine gradient, Nature (London) **503**, 285 (2013).

[50] G. Venkiteswaran, S. W. Lewellis, J. Wang, E. Reynolds, C. Nicholson, and H. Knaut, Generation and dynamics of an endogenous, self-generated signaling gradient across a migrating tissue, Cell **155**, 674 (2013).

[51] L. Tweedy, D. A. Knecht, G. M. Mackay, and R. H. Insall, Self-generated chemoattractant gradients: Attractant depletion extends the range and robustness of chemotaxis, PLoS Biol. **14**, e1002404 (2016).

[52] J. Stock, T. Kazmar, F. Schlumm, E. Hannezo, and A. Pauli, A self-generated toddler gradient guides mesodermal cell migration, Sci. Adv. **8**, eadd2488 (2022).

[53] M. C. Uçar, Z. Alsberga, J. Alanko, M. Sixt, and E. Hannezo, Self-generated chemotaxis of mixed cell populations, Proc. Natl. Acad. Sci. USA **122**, e2504064122 (2025).

[54] A. Shellard and R. Mayor, Collective durotaxis along a self-generated stiffness gradient in vivo, Nature (London) **600**, 690 (2021).

[55] A. A. Fragkopoulos, J. Vachier, J. Frey, F.-M. Le Menn, M. G. Mazza, M. Wilczek, D. Zwicker, and O. Bäumchen, Self-generated oxygen gradients control collective aggregation of photosynthetic microbes, J. R. Soc. Interface **18**, 20210553 (2021).

[56] A. Ancel, H. Visser, Y. Handrich, D. Masman, and Y. L. Maho, Energy saving in huddling penguins, Nature (London) **385**, 304 (1997).

[57] A. Ancel, C. Gilbert, N. Poulin, M. Beaulieu, and B. Thierry, New insights into the huddling dynamics of emperor penguins, Anim. Behav. **110**, 91 (2015).

[58] A. V. Zampetaki, B. Liebchen, A. V. Ivlev, and H. Löwen, Collective self-optimization of communicating active particles, Proc. Natl. Acad. Sci. USA **118**, e2111142118 (2021).

[59] D. Ghosh, B. Chakrabarti, and X. Cheng, Source data and simulation code for "Density-controlled reversal of collective migration in bacterial aerotaxis", Zenodo, 2026, https://doi.org/10.5281/zenodo.20048642.

[60] W. Niblack, *An Introduction to Digital Image Processing* (Strandberg Publishing Company, Birkerød, Denmark, 1985).

[61] L. A. Segel, Incorporation of receptor kinetics into a model for bacterial chemotaxis, J. Theor. Biol. **57**, 23 (1976).

[62] D. Grünbaum, Advection-diffusion equations for internal state-mediated random walks, SIAM J. Appl. Math. **61**, 43 (2000).

[63] B. C. Mazzag, *Mathematical Models in Biology* (University of California, Davis, 2002).